


Dynamics of soap bubble inflation

Saini Jatin Rao , Siddhant Jain , and Saptarshi Basu *

Department of Mechanical Engineering, Indian Institute of Science, Bengaluru 560012, India



(Received 9 February 2024; accepted 23 April 2024; published 28 May 2024)

Bubbles have always captivated our curiosity with their aesthetics and complexities alike. While the act of blowing bubbles is familiar to everyone, the underlying physics of these fleeting spheres often eludes reasoning. In this Letter, we discuss the dynamics of inflating a soap bubble using controlled airflow through a film-coated nozzle. We assess and predict the rate of inflation by varying the source pressure. Visualizing the previously unexplored internal flow reveals that air enters the bubble as a round jet, emerging from the nozzle opening and impinges on the expanding concave bubble interface to form a toroidal vortex. Several scaling laws of the associated vortical flow spanning the entire bubble and the vortex core are reported. The observed dynamics of this bubble-confined vortex ring formation indicate universality in certain aspects when compared to the free laminar vortex rings.

DOI: [10.1103/PhysRevFluids.9.L051602](https://doi.org/10.1103/PhysRevFluids.9.L051602)

Introduction. Soap bubbles have been a source of wonder for researchers and the general public alike for generations, yet our continued exploration still unveils nuances that keep us engaged with these iridescent objects [1]. Among these exciting features are the vivid interference patterns [2], bursting films [3], minimal surfaces [4], and even the demonstration of a soap bubble as an optical cavity to generate a laser [5]. This Letter specifically delves into the physics of soap bubble inflation, revealing the remarkable flow that happens inside. Notably, the internal flow exhibits a toroidal vortex structure as illustrated in Fig. 1.

The dynamics associated with bubble inflation have been examined from different perspectives throughout the literature. In the most general sense, the soap bubble anatomy consists of a thin film of soap liquid stretching against a gas flow. This soap film is usually pinned or held over an aperture through which the air is introduced, enabling the inflation process. The aperture can be a ring or a wand, where a free jet or stream of gas is used for blowing the bubble [6–9]. Another possibility is a closed configuration where an opening at the tube end with the gas efflux is the aperture over which the soap film is pinned [10]. These studies primarily focused on the motion or stretching of the soap film. It has been shown that in the case of blowing using a free gas jet, there exists a critical velocity beyond which a bubble forms and detaches from a soap film [6,7]. Blowing a bubble through a constriction in a fixed mass system depicts an unstable growth of the bubble interface [10]. However, beyond these considerations, the associated internal flow structure of the gas phase being used for inflation is rarely explored or reported.

The soap films were also extended to study two-dimensional flows where the incumbent vortical dynamics were rigorously observed and studied for the flowing film [11,12] and bubbles [13,14]. This study, however, focuses on the vortical dynamics of the gas phase flow within a growing soap bubble.

* Also at Interdisciplinary Centre of Energy Sciences, Indian Institute of Science, Bengaluru 560012, India; sbasu@iisc.ac.in

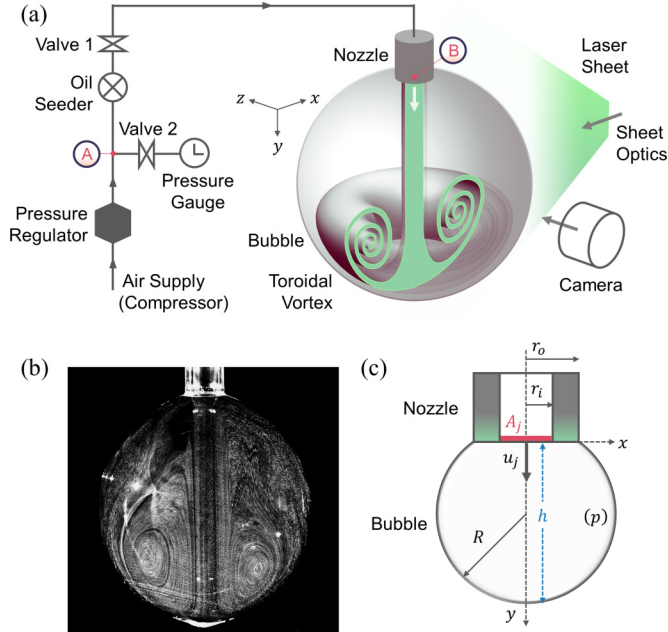


FIG. 1. (a) A schematic of the experimental setup for inflating a soap bubble with an air supply at a prescribed pressure, seeded with olive oil droplets. A laser sheet is used to illuminate these particles for flow visualisation captured through a high-speed camera. (b) Long exposure image of the flow within the bubble during inflation depicting vortex structure. (c) Nomenclature associated with the nozzle (inner radius r_i , outer radius r_o , jet area A_j), bubble geometry (spherical cap radius R , height h), and airflow (jet velocity u_j , static gauge pressure inside bubble $p = 4\sigma/R$, where σ is air-soap interface surface tension).

The anatomy of an inflating bubble can be extended to other systems where a membrane or interface is stretched against a fluid flow. This involves problems spanning from filling a simple rubber balloon [15] to the flow focusing within microdroplets [16]. Containers like plastic bottles or glass vessels are produced by blow moulding, i.e., inflating a plug in a mould of a prescribed shape, where flow-induced cooling depends on the internal fluid motion [17]. Soft robotics and medical devices [18] involve controlled inflation and deflation of tubes, balloons, or chambers, where a uniform flow and pressure distribution might be necessary. Furthermore, the membrane-based systems involving engulfment flows induced by forced membrane motion will also depict similar flow characteristics. The jellyfish-like locomotion [19,20], the flow inside the heart chambers [21], or even artificial organs are a few examples.

For the aforementioned systems, the precise knowledge of internal flow dynamics of the fluid phase enclosed within a membrane-like entity is deemed necessary for a better understanding and control of the associated phenomenon. The exact flow conditions will differ vastly from our canonical bubble inflation problem; however, a prominent vortical structure is usually associated, either due to fluid-structure interaction or unsteady inlet flow conditions. This problem thus casts a basis for a class of problems involving a confined, unsteady toroidal vortex continually being fed with a mass flux, unlike the traditional self-propelled free vortex rings, where the feeding is discontinued after it pinches off from the orifice [22,23].

In the current exposition, we consider inflating a soap bubble by expanding a soap film deposited at the tube end opening with air. The first part of the study looks into the dynamics associated with the soap film motion and uses first principles to deduce the scaling laws for the bubble growth rate. The second part delves further into the internal airflow dynamics within this growing bubble. The incoming airflow conforms into a toroidal vortex initially. Eventually, as the bubble grows,

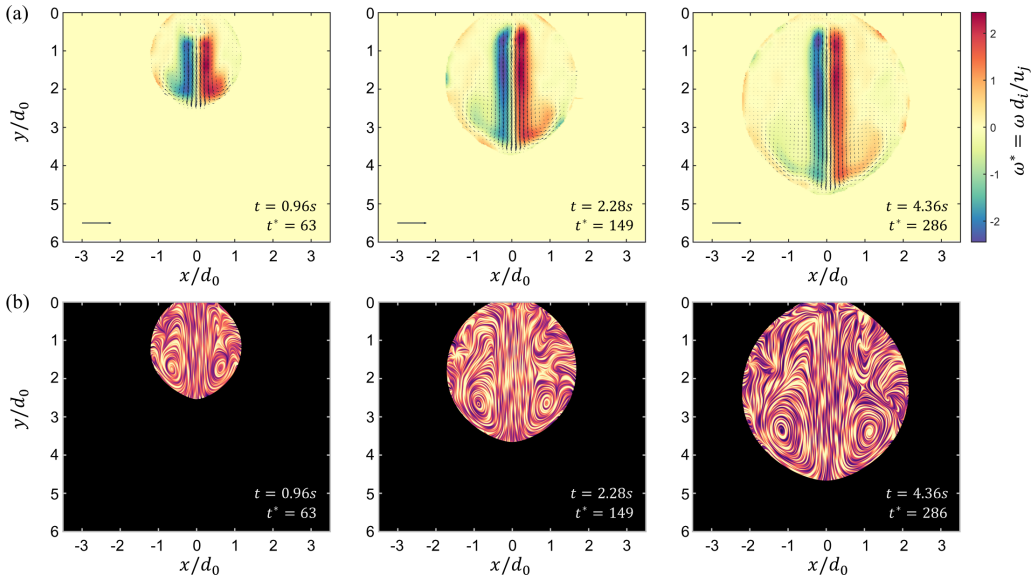


FIG. 2. (a) Vorticity and vector fields associated with internal flow of an inflating bubble at various normalized time instances for the case of dimensionless source pressure $\tilde{p}_0 \approx 28$ or equivalently $p_0 = 646Pa$ (b) LIC (Line Integral Convolution) flow visualization for the same flow instances.

air enters as a round jet which impinges on the concave bubble surface, forming a wall jet that eventually separates to form a localized toroidal vortical structure (see Figs. 2, 3, and movies 1–6 in the Supplemental Material [24]).

Experiments. The schematic of the experimental setup is depicted in Fig. 1(a). Air supply at a constant pressure from the reservoir is utilized for bubble inflation, where the downstream pressure

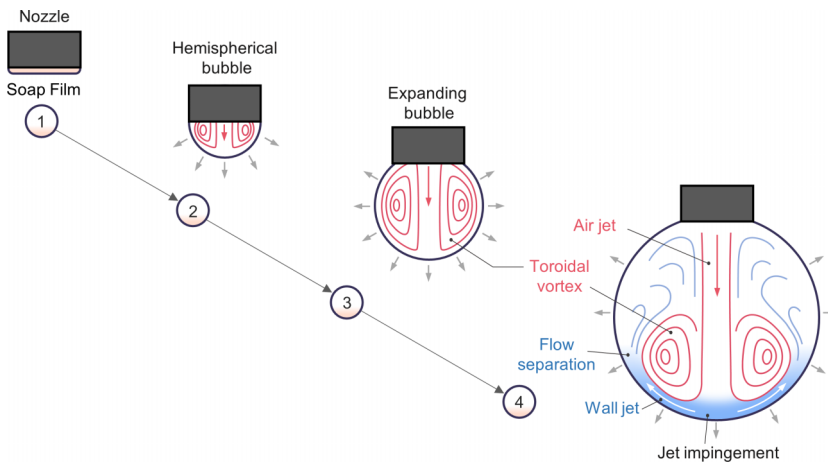


FIG. 3. A schematic depicting the sequence of events for a soap bubble inflation. (1) Thin film deposited over the nozzle aperture. (2) Film expansion induced by airflow leading to hemispherical bubble. (3) Bubble growth conforming a spherical cap with the gas phase flow within, depicting a toroidal vortex spanning the whole volume. (4) Further film expansion with the incoming round air jet impinging on bubble interior, developing a wall jet which separates to form a localized vortex.

is controlled using a pressure regulator. A seeder arrangement in line with the flow circuit introduces olive oil droplets of size $\sim 1\text{--}5\ \mu\text{m}$, which is essential for internal airflow visualisation during bubble blowing. A manometric gauge is used for pressure measurement between the regulator and the seeder. Through valve ‘1’ and PU tubes, the output of this apparatus is connected to an acrylic nozzle at the other end having inner and outer diameters of $d_i = 2r_i = 6\ \text{mm}$ and $d_o = 2r_o = 10\ \text{mm}$, respectively. To generate a soap bubble, the nozzle is dipped in a soap solution (Commercial - Bubble Magic) to deposit a soap film at the opening. For repeatability, the nozzle tip is dipped to approximately the same depth of $\sim 1\text{--}2\ \text{mm}$ for each run, and the nozzle end is held within a large acrylic enclosure. Valve ‘2’ is closed, and valve ‘1’ is opened during the inflation process, where the input pressure is preadjusted through the regulator. To measure the actual stagnation pressure just after the regulator, valve ‘1’ is closed, and valve ‘2’ is opened after every run. The pressure measured through the manometer is then considered an equivalent source supply pressure for the system. The air-liquid surface tension $\sigma = 28.56\ \text{mN/m}$ of the soap solution was measured using the pendant droplet method, and viscosity $\eta_1 = 132.49\ \text{mPa s}$ was determined using an Anton Paar model rheometer.

The flow visualization is achieved using a high-speed dual pulsed Nd:YLF laser (pulse energy of 30 mJ, emission wavelength 527 nm, Photonics, Inc.), where a laser sheet from a cylindrical lens is passed through the symmetry axis of the bubble and tube system. The images of the illuminated seeded particles for particle image velocimetry (PIV) were captured at 95 frames per second, using a high-speed camera (Photron Mini UX) at a pixel resolution of 1280×1024 pixels with a field of view of $86 \times 70\ \text{mm}$. The outlines of the bubble interfaces in these images [see Fig. 1(b)] were used to determine the geometrical parameters like height h and radius R , considering the bubble to be a spherical cap pinned over the outer edge of the nozzle. The associated nomenclature is depicted in Fig. 1(c).

For PIV, the images were post-processed in Davis 8.4 software to obtain the velocity field of the internal flow. This involves a cross-correlation technique with a constant multipass interrogation window of size 32×32 pixels with 50% overlap. The velocity vectors and the vorticity field for a particular source pressure at different normalised time instances are depicted in Fig. 2(a) (these normalized parameters are defined later). The Line Integral Convolution (LIC) representation [25] depicting streamline-like features in a continuous fashion is illustrated in Fig. 2(b). Two counter-rotating vortices are clearly visible in Fig. 2, portraying a dominant toroidal vortex engulfed within the bubble. The internal flowfield hence obtained will be utilised to assess the vorticity dynamics.

A phenomenological sequence of events for the inflation process is depicted in Fig. 3. Bubble inflation is achieved from the tube end with a soap film deposited at the opening. Initially, the incoming air fills the bubble volume, and the flow conforms to the concave confinement within the expanding film. The bubble is eventually hemispherical with a minimum radius of curvature and grows in radius later with further inflation. The internal flow forms a toroidal vortex, which spans the small bubble volume initially. Later, as the bubble grows, the incoming air assumes a round jet form. This laminar jet impinges the soap film at the other end of the bubble, forming a wall jet that moves along the curved inner surface of the bubble. This wall jet eventually separates to form a toroidal vortical structure engulfed within a growing bubble.

Inflation dynamics. To emulate bubble inflation, a simple model based on Bernoulli’s principle is employed. Applying this between points (A) and (B) [refer to Fig. 1(a)] gives a simple equation for airflow from the source to the bubble as

$$p_0 = \frac{4\sigma}{R} + \frac{1}{2}\rho_a u_j^2 + \Delta p_{\text{loss}}, \quad (1)$$

where R is the radius of the bubble considered to be as the spherical cap, p_0 is the stagnation gauge pressure at source [measured at (A) in Fig. 1(a)], ρ_a is the air density and σ is the air-soap interface surface tension. The term $4\sigma/R$ represents the Laplace pressure and is assumed to be uniform static pressure within the bubble, including the nozzle exit (B) [see Fig. 1(a)]. The average air jet velocity u_j at the nozzle exit can be expressed in terms of the volumetric flow rate

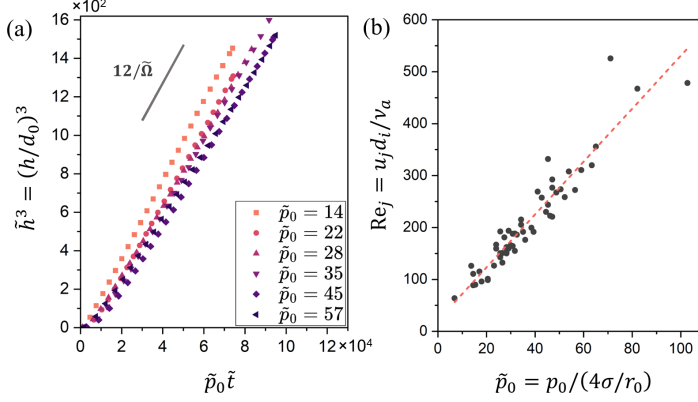


FIG. 4. (a) Growth of normalized bubble height \tilde{h}^3 with a modified dimensionless time $\tilde{p}_0 \tilde{t}$ taking into account the source pressure, indicating linear variation of bubble volume with time. (b) Steady-state air jet Reynolds number depicting a linear correlation with the dimensionless source pressure.

Q and exit area A_j as $u_j = Q/A_j$. Δp_{loss} is the viscous pressure loss along the pipe and can be expressed as $\Delta p_{\text{loss}} = \Omega Q$, where Ω is the equivalent frictional resistance for the piping system. For a given setup, the experimental parameter Ω should be roughly the same. For a Poiseuille's pipe flow $\Omega \sim \frac{8\pi\mu_a L_{\text{eff}}}{A_{\text{eff}}^2}$, where μ_a is the air viscosity; L_{eff} and A_{eff} are the effective length and cross-sectional area for the piping system, respectively. Eq. (1) can be further simplified to obtain an expression for Q , which can be equated to the rate of increase in the bubble volume using mass balance. On simplification, the expression for the dimensionless version of the bubble height \tilde{h} [see Fig. 1(c) for bubble and nozzle geometry details] is obtained as

$$\frac{d\tilde{h}}{d\tilde{t}} = \frac{1}{1 + \tilde{h}^2} \left\{ -\tilde{\Omega} + \sqrt{\tilde{\Omega}^2 + 8 \left(\tilde{p}_0 - \frac{2\tilde{h}}{1 + \tilde{h}^2} \right)} \right\}, \quad (2)$$

where $\tilde{h} = \frac{h}{r_0}$, $\tilde{t} = \frac{t}{\tau}$ with time-scale $\tau = \frac{\pi}{2} \sqrt{\frac{\rho_a r_0^2}{A_j^2 \sigma}}$, $\tilde{\Omega} = \Omega \sqrt{\frac{A_j^2 r_0}{\rho_a \sigma}}$, and $\tilde{p}_0 = \frac{p_0}{4\sigma/r_0}$. In the experiments, we observe a linear growth of the bubble volume with time, except for a very short early phase. In the limit of a large bubble $\tilde{h} \gg 1$, $h \approx 2R$ and Eq. (2) approximates to

$$\tilde{h}^3 \approx \frac{12}{\tilde{\Omega}} \tilde{p}_0 \tilde{t}. \quad (3)$$

A derivation for Eqs. (2) and (3) is presented in the Supplemental Material [24]. The experimental data considered in the dimensionless form is hence plotted in Fig. 4(a); a dimensional counterpart for which is also depicted in the Supplemental Material (Fig. S1 [24]). \tilde{h}^3 varies linearly with a modified dimensionless time $\tilde{p}_0 \tilde{t}$ taking into account the source pressure, as expected from Eq. (3). The curves overlap and the slopes at various pressures assimilate to give a fairly constant $\tilde{\Omega} \approx 600$, validating our model. This dimensionless resistance agrees with the prediction from Poiseuille's hypothesis within the order of magnitude. Furthermore, as the bubble volume $V_b \propto \tilde{h}^3$, the slope $dh^3/dt \propto Q \propto u_j$ [24]. The rate of the bubble volume growth observed in the experiments was therefore used to evaluate the air jet velocity, which agrees with the PIV results within an error margin of 10%. The air jet velocity is unsteady only in the early phase of inflation, and a steady state is approached as the bubble grows, i.e., the radius R increases and the opposing Laplace pressure within the bubble diminishes. Defining the air jet Reynolds number as $\text{Re}_j = u_j d_i / \nu_a$, from Eq. (3), $\text{Re}_j \propto \tilde{p}_0$. The linear correlation is observed in the experimental realisations as depicted in Fig. 4(b). From this

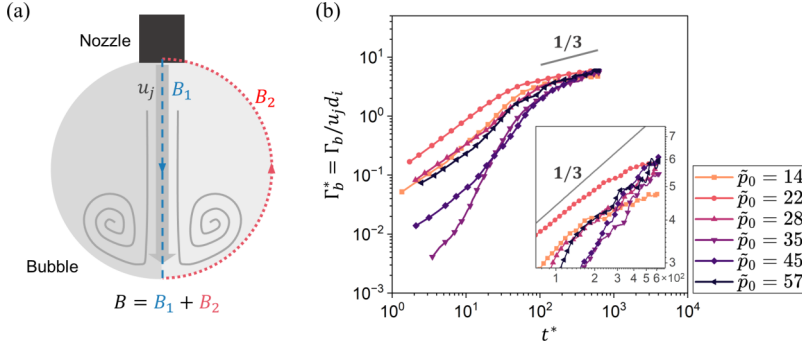


FIG. 5. (a) Contour B for bubble circulation evaluation from experimental data. This contour can be segmented into B_1 (dashed lines) and B_2 (dotted lines) for simplified analysis. (b) Variation of the dimensionless bubble circulation with time depicting the scaling $\Gamma_b^* \sim t^{1/3}$. The inset illustrates an enlarged view of this scaling.

analysis and experimental observations, we deduce the scaling for the bubble radius with time as $h \sim R \sim t^{1/3}$ for inflation using a constant pressure supply. The phenomenon was investigated within the range $Re_j = 50\text{--}500$ and a corresponding Weber number range of $We = 0.02\text{--}0.5$, following the definition $We = \rho_a u_j^2 d_0 / \sigma$.

Vortical dynamics. The flow inside the bubble depicts a fascinating toroidal vortex structure as depicted in Fig. 2. The vortical flow spans the whole bubble volume and is similar to a Hill's vortex [26] in the early phase when the bubble is small as depicted in Fig. 3. Impingement of the incoming round jet later forms a wall jet at the expanding concave interface, which separates eventually and rolls up to form a vortex localized to the lower part of the bubble as it grows (see Figs. 2 and 3). The incoming jet feeds mass to this growing vortex and the bubble as a whole.

The velocity vector field obtained from PIV is analysed to understand the vortical dynamics associated with the internal flow. The circulation Γ_b associated with the flow inside the bubble is deduced for the right half within the contour B as depicted in Fig. 5(a) using $\Gamma_b = \int_B \omega \, dA$. The variation of the dimensionless circulation enclosed within bubble $\Gamma_b^* = \frac{\Gamma_b}{u_j d_i}$ with time $t^* = tu_j/d_i$ is depicted in Fig. 5(b). We observe the scaling $\Gamma_b^* \sim t^{1/3}$ in the later stages of inflation. This can be deduced by dividing the contour B into two segments B_1 and B_2 as depicted in Fig. 5(a). Then the circulation can be also expressed as $\Gamma_b = \int_{B_1} \mathbf{u} \cdot d\mathbf{l} + \int_{B_2} \mathbf{u} \cdot d\mathbf{l}$, where it can be shown that $\int_{B_1} \mathbf{u} \cdot d\mathbf{l} \gg \int_{B_2} \mathbf{u} \cdot d\mathbf{l}$ and $\int_{B_1} \mathbf{u} \cdot d\mathbf{l} \sim u_j h$ [24]. As the height $h \sim t^{1/3}$ when the bubble is large, this predicts the observed scaling $\Gamma_b \sim t^{1/3}$. However, a slight deviation from this scaling can be observed for lower source pressure cases, depicted in the inset of Fig. 5(b). This is anticipated because, for the large bubble limit, it was assumed that the centerline air jet velocity would be uniform with a small portion at the bottom over which stagnation occurs, which may not be true for incoming jets with lower momentum (or Re_j). Also, effects like coupling between the airflow and thin film flow associated with liquid film stretching during inflation and draining induced by gravity were neglected, which may affect the proposed scaling. The air wall jet may impose shear stress and forced convection over the soap film, affecting film drainage, evaporation rate, stability, and lifetimes of these bubbles.

The incoming jet from the nozzle has a dominant shear layer with large vorticity, contributing significantly to the bubble circulation evaluated earlier. In general, a large vorticity value does not necessarily represent a vortex core region [27]. Therefore, the overall bubble circulation may not adequately describe the dynamics associated with the core. The evolution of coherent structures like a vortex core typically governs the interaction dynamics for various flow phenomena including mixing, entrainment, heat transfer, and turbulence. Henceforth, the vortex identification schemes were implemented to isolate the core for further analysis. The Γ_2 criteria [28] was used to identify

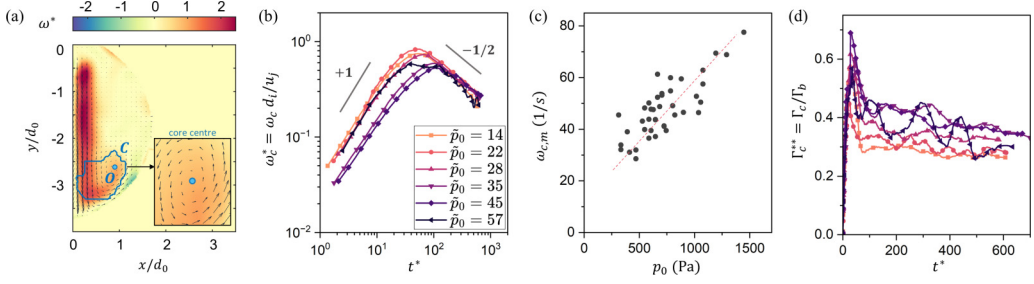


FIG. 6. (a) The contour C depicting the connected region identified as core using the swirl strength (λ_{ci}) criteria with core center O determined from the Γ_2 method. (b) Variation of the dimensionless average core vorticity ω_c^* with normalized time t^* depicting the scaling $\omega_c^* \sim t^{*-1/2}$. (c) Peaks in the variation of average core vorticity $\omega_{c,m}$ correlated linearly with the source pressure p_0 . (d) Variation of dimensionless core circulation Γ_c^{**} with normalized time t^* depicting it approaches a constant value.

the location of the prominent core O , and the associated core region C was determined using swirl strength or λ_{ci} criteria [29], as depicted in Fig. 6(a). The Γ_2 criteria inspects the relative orientation of velocity vectors in the neighborhood of a point to identify the core center, and the λ_{ci} criteria determines the core region based on the imaginary part of the eigenvalues of the velocity gradient tensor. A brief discussion of these techniques can be found in the Supplemental Material [24]. The core dynamics is assessed through the average vorticity, defined as $\omega_c = \int_C \omega dA / \int_C dA$ and circulation $\Gamma_c = \int_C \omega dA$. The variation of normalised average core vorticity $\omega_c^* = \frac{\omega_c}{u_j/d_i}$ with time $t^* = tu_j/d_i$ is depicted in Fig. 6(b). We observe the scaling $\omega_c^* \sim t^{*-1/2}$ after the peak core vorticity is reached. A simple explanation is obtained by scaling vorticity to the velocity gradients where incoming jet velocity u_j serves as a suitable scale along with a characteristic length scale associated with the core l_c such that $\omega_c \sim u_j/l_c$. The identified core C spans the swirling region in the neighborhood of the core center O [depicted in the inset of Fig. 6(a)] to the high shear region in the vicinity of the impingement where the jet turns and spreads along the concave soap film. Although from the vector field visualization, a vortical structure is not apparent in this impingement region, the eigenvalues of velocity gradient tensor (from λ_{ci} criteria), however, predict a dominant rotational component. This unsteady stagnation point flow and the overall recirculatory flow associated with the wall jet separation contribute to core dynamics. Essentially, the wall jet feeds this vortex, and hence, the viscous length scale $l_c \sim \sqrt{\nu a t}$ is suitable to characterise the vortical dynamics of the core [30,31]. Therefore, $\omega_c \sim u_j/\sqrt{\nu a t}$, which explains the observed scaling $\omega_c \sim t^{-1/2}$ and the peak associated with the core vorticity variation $\omega_{c,m} \propto u_j \propto p_0$ [see Figs. 6(b) and 6(c)]. There is an anticipated flow transition around this peak delineating the flow into two broad regimes, i.e., prior and post wall jet separation, as indicated in Fig. 3. Before the peak, the average core vorticity depicts an increasing trend and roughly follows the scaling $\omega_c^* \sim t^*$. This transition in flow dynamics and associated scaling is apparent in Figs. 5(b) and 6(b), which happens around $t^* \sim \mathcal{O}(10^2)$.

The core circulation is normalized using the bubble circulation such that $\Gamma_c^{**} = \Gamma_c/\Gamma_b$. The variation is depicted in Fig. 6(d), where it is observed that this dimensionless core circulation approaches a constant value with time, which means that the core circulation eventually follows a scaling law similar to the bubble circulation.

In the initial phase of inflation, core vorticity and circulation depict an increasing trend prior to the wall jet separation, presumably due to flow confinement. This leads to a prominent rotational flow, which spans the whole bubble volume. Hence, a coupled growth of bubble size and vortical characteristics is observed until the point where the flow starts to separate. After this, the core vorticity starts to decay. Also, the initial phase is unsteady, with the bottom-most point of the bubble accelerating significantly. In the later stages, the jet impingement is relatively steadier. The average core vorticity of this confined vortex depicts a scaling law $\omega_c^* \sim t^{*-1/2}$ independent of the bubble

growth rate. The core circulation, when normalized with the overall bubble circulation Γ_c^{**} , depicts a variation qualitatively similar to that of a free vortex ring formation [22,32] where it increases rapidly, then achieves a constant value. In earlier studies, this ratio approached a value of 0.4–0.6 for free laminar vortex rings, where the total circulation of the half-vortex, including the trailing jet, was used for normalization. This is similar to what is observed in the current study. Thus, in a sense, the bubble-confined unsteady vortex ring under consideration here also retains these universal characteristics associated with the generation of a free laminar vortex ring. Although the primary source of vorticity generation is the boundary layer at the inner tube walls in the former case [33], and the wall jet on the moving bubble interface acts as an additional source in the latter. To have a better understanding of the universality of the vortical dynamics, further research is required into the initial unsteady phase where the wall jet separation starts and sustains.

Furthermore, the jet impingement here differs from the conventional free jet impingement [34,35] or vortex impingement [36] studies in terms of the confinement imposed by the bubble interface. The consequences include the imposed entrainment and the vortex interacting with the jet itself. The jet eventually becomes unstable as these effects become prominent for a higher Reynolds number jet. This phenomenon is depicted in the Supplemental Material [24].

Conclusion. In closing, we have discussed the dynamics associated with an inflating soap bubble and the associated internal flow, where we deduce several universal scaling laws associated with the bubble growth and the prominent vortex that forms within. The bubble volume is found to grow linearly in time with the bubble height following the scaling $\tilde{h}^3 \sim \tilde{p}_0 \tilde{t}$. The bubble circulation follows the scaling $\Gamma_b^* \sim t^{*1/3}$ and the average core vorticity depicts $\omega_c^* \sim t^{*-1/2}$. The phenomenon occurs prominently due to the round jet impingement with the bubble interface and was investigated within the range $Re_j = 50\text{--}500$. The universality extending from a free vortex ring formation, vortical dynamics of the initial phase and the jet instability induced in the later phases are among the compelling observations that are to be examined further.

Acknowledgments. S.J.R. and S.J. would like to thank the Prime Minister Research Fellowship (PMRF) for the financial support. S.B. would like to thank the support from the Pratt and Whitney Chair professorship.

-
- [1] C. V. Boys, *Soap Bubbles, Their Colours and the Forces which Mold Them* (Dover Publications, New York, 1959).
 - [2] N. S. Lalli and A. Giusti, Coherence effects on the interference colors of soap films, *J. Appl. Phys.* **134**, 093103 (2023).
 - [3] H. Lhuissier and E. Villermaux, Soap films burst like flapping flags, *Phys. Rev. Lett.* **103**, 054501 (2009).
 - [4] L. Giomi and L. Mahadevan, Minimal surfaces bounded by elastic lines, *Proc. R. Soc. A* **468**, 1851 (2012).
 - [5] Z. Korenjak and M. Humar, Smectic and soap bubble optofluidic lasers, *Phys. Rev. X* **14**, 011002 (2024).
 - [6] L. Salkin, A. Schmit, P. Panizza, and L. Courbin, Generating soap bubbles by blowing on soap films, *Phys. Rev. Lett.* **116**, 077801 (2016).
 - [7] M. Zhou, M. Li, Z. Chen, J. Han, and D. Liu, Formation of soap bubbles by gas jet, *Appl. Phys. Lett.* **111**, 241604 (2017).
 - [8] C. A. E. Hamlett, D. N. Boniface, A. Salonen, E. Rio, C. Perkins, A. Clark, S. Nyugen, and D. J. Fairhurst, Blowing big bubbles, *Soft Matter* **17**, 2404 (2021).
 - [9] L. Ganedi, A. U. Oza, M. Shelley, and L. Ristroph, Equilibrium shapes and their stability for liquid films in fast flows, *Phys. Rev. Lett.* **121**, 094501 (2018).
 - [10] M. Grosjean and E. Lorenceau, Unstable growth of bubbles from a constriction, *Phys. Rev. Fluids* **8**, 053602 (2023).
 - [11] P. Vorobieff, M. Rivera, and R. E. Ecke, Soap film flows: Statistics of two-dimensional turbulence, *Phys. Fluids* **11**, 2167 (1999).
 - [12] P. Roushan and X. L. Wu, Universal wake structures of Kármán vortex streets in two-dimensional flows, *Phys. Fluids* **17**, 073601 (2005).

- [13] F. Seychelles, Y. Amarouchene, M. Bessafi, and H. Kellay, Thermal convection and emergence of isolated vortices in soap bubbles, *Phys. Rev. Lett.* **100**, 144501 (2008).
- [14] T. Meuel, Y. L. Xiong, P. Fischer, C. H. Bruneau, M. Bessafi, and H. Kellay, Intensity of vortices: From soap bubbles to hurricanes, *Sci. Rep.* **3**, 3455 (2013).
- [15] D. Ilssar and A. D. Gat, On the inflation and deflation dynamics of liquid-filled, hyperelastic balloons, *J. Fluids Struct.* **94**, 102936 (2020).
- [16] S. A. Vagner, S. A. Patlazhan, C. A. Serra, and D. Funfschilling, Vortex flow evolution in a growing microdroplet during co-flow in coaxial capillaries, *Phys. Fluids* **33**, 072010 (2021).
- [17] J. Zimmer, G. Chauvin, and M. Stommel, Experimental investigation and numerical simulation of liquid supported stretch blow molding, *Polymer Eng. Sci.* **55**, 933 (2015).
- [18] L. Manfredi, E. Capoccia, G. Ciuti, and A. Cuschieri, A soft pneumatic inchworm double balloon (SPID) for colonoscopy, *Sci. Rep.* **9**, 11109 (2019).
- [19] J. H. Costello, S. P. Colin, J. O. Dabiri, B. J. Gemmell, K. N. Lucas, and K. R. Sutherland, The hydrodynamics of jellyfish swimming, *Ann. Rev. Marine Sci.* **13**, 375 (2021).
- [20] M. Baskaran and K. Mulleners, Lagrangian analysis of bio-inspired vortex ring formation, *Flow* **2**, E16 (2022).
- [21] G. Di Labbio, J. Vétel, and L. Kadem, Material transport in the left ventricle with aortic valve regurgitation, *Phys. Rev. Fluids* **3**, 113101 (2018).
- [22] M. Gharib, E. Rambod, and K. Shariff, A universal time scale for vortex ring formation, *J. Fluid Mech.* **360**, 121 (1998).
- [23] M. Krieg and K. Mohseni, A new kinematic criterion for vortex ring pinch-off, *Phys. Fluids* **33**, 037120 (2021).
- [24] See Supplemental Material at <http://link.aps.org/supplemental/10.1103/PhysRevFluids.9.L051602> for the derivation of the expressions for the bubble geometry evolution and the enclosed circulation; brief discussion on the vortex core identification schemes; instability observed in the jet at higher Reynolds numbers; supplementary movies 1–6 depicting internal airflow visualisation in bubbles during inflation and their respective descriptions. The Supplemental Material also contains Refs. [27–29].
- [25] B. Cabral and L. C. Leedom, Imaging vector fields using line integral convolution, in *Proceedings of the 20th Annual Conference on Computer Graphics and Interactive Techniques* (ACM, Anaheim CA, 1993), pp. 263–270.
- [26] M. J. M. Hill and O. M. F. E. Henrici, VI. On a spherical vortex, *Philos. Trans. Roy. Soc. London A* **185**, 213 (1997).
- [27] J. Jeong and F. Hussain, On the identification of a vortex, *J. Fluid Mech.* **285**, 69 (1995).
- [28] L. Graftieux, M. Michard, and N. Grosjean, Combining PIV, POD and vortex identification algorithms for the study of unsteady turbulent swirling flows, *Meas. Sci. Technol.* **12**, 1422 (2001).
- [29] J. Zhou, R. J. Adrian, S. Balachandar, and T. M. Kendall, Mechanisms for generating coherent packets of hairpin vortices in channel flow, *J. Fluid Mech.* **387**, 353 (1999).
- [30] C. Tung and L. Ting, Motion and decay of a vortex ring, *Phys. Fluids* **10**, 901 (1967).
- [31] J. J. Allen and M. S. Chong, Vortex formation in front of a piston moving through a cylinder, *J. Fluid Mech.* **416**, 1 (2000).
- [32] M. Rosenfeld, E. Rambod, and M. Gharib, Circulation and formation number of laminar vortex rings, *J. Fluid Mech.* **376**, 297 (1998).
- [33] P. S. Krueger, An over-pressure correction to the slug model for vortex ring circulation, *J. Fluid Mech.* **545**, 427 (2005).
- [34] J. M. Berghorson, K. Sone, T. W. Mattner, P. E. Dimotakis, D. G. Goodwin, and D. I. Meiron, Impinging laminar jets at moderate Reynolds numbers and separation distances, *Phys. Rev. E* **72**, 066307 (2005).
- [35] P. Aillaud, L. Y. M. Gicquel, and F. Duchaine, Investigation of the concave curvature effect for an impinging jet flow, *Phys. Rev. Fluids* **2**, 114608 (2017).
- [36] T. Ahmed and B. D. Erath, Experimental study of vortex ring impingement on concave hemispherical cavities, *J. Fluid Mech.* **967**, A38 (2023).